

Real-time imaging of cardiovascular dynamics and circulating gold nanorods with multispectral optoacoustic tomography

Adrian Taruttis, Eva Herzog, Daniel Razansky*,
and Vasilis Ntziachristos

*Institute for Biological and Medical Imaging, Technical University of Munich and Helmholtz Center Munich,
Ingolstädter Landstraße 1, 85764 Neuherberg, Germany*

**dr@tum.de*

Abstract: Macroscopic visualization of functional and molecular features of cardiovascular disease is emerging as an important tool in basic research and clinical translation of new diagnostic and therapeutic strategies. We showcase the application of Multispectral Optoacoustic Tomography (MSOT) techniques to noninvasively image different aspects of the mouse cardiovascular system macroscopically in real-time and *in vivo*, an unprecedented ability compared to optical or optoacoustic (photoacoustic) imaging approaches documented so far. In particular, we demonstrate imaging of the carotid arteries, the aorta and the cardiac wall. We further demonstrate the ability to dynamically visualize circulating gold nanorods that can be used to enhance contrast and be extended to molecular imaging applications. We discuss the potential of this imaging ability in cardiovascular disease (CVD) research and clinical applications.

©2010 Optical Society of America

OCIS codes: (170.5120) Photoacoustic imaging; (110.4234) Multispectral and hyperspectral imaging; (170.3880) Medical and biological imaging.

References and links

1. R. A. Kruger, W. L. Kiser, D. R. Reinecke, G. A. Kruger, and K. D. Miller, "Thermoacoustic molecular imaging of small animals," *Mol. Imaging* **2**(2), 113–123 (2003).
2. M. Xu, and L. V. Wang, "Photoacoustic imaging in biomedicine," *Rev. Sci. Instrum.* **77**(4), 041101 (2006).
3. K. Maslov, G. Stoica, and L. V. Wang, "In vivo dark-field reflection-mode photoacoustic microscopy," *Opt. Lett.* **30**(6), 625–627 (2005).
4. R. J. Zemp, L. Song, R. Bitton, K. K. Shung, and L. V. Wang, "Realtime photoacoustic microscopy of murine cardiovascular dynamics," *Opt. Express* **16**(22), 18551–18556 (2008).
5. X. Wang, Y. Pang, G. Ku, X. Xie, G. Stoica, and L. V. Wang, "Noninvasive laser-induced photoacoustic tomography for structural and functional in vivo imaging of the brain," *Nat. Biotechnol.* **21**(7), 803–806 (2003).
6. S. Manohar, S. E. Vaartjes, J. C. G. van Hespén, J. M. Klaase, F. M. van den Engh, W. Steenbergen, and T. G. van Leeuwen, "Initial results of in vivo non-invasive cancer imaging in the human breast using near-infrared photoacoustics," *Opt. Express* **15**(19), 12277–12285 (2007).
7. J. J. Niederhauser, M. Jaeger, R. Lemor, P. Weber, and M. Frenz, "Combined ultrasound and optoacoustic system for real-time high-contrast vascular imaging in vivo," *IEEE Trans. Med. Imaging* **24**(4), 436–440 (2005).
8. K. Maslov, H. F. Zhang, S. Hu, and L. V. Wang, "Optical-resolution photoacoustic microscopy for in vivo imaging of single capillaries," *Opt. Lett.* **33**(9), 929–931 (2008).
9. F. Kiessling, D. Razansky, and F. Alves, "Anatomical and microstructural imaging of angiogenesis," *Eur. J. Nucl. Med. Mol. Imaging* (2010).
10. J. Laufer, D. Delpy, C. Elwell, and P. Beard, "Quantitative spatially resolved measurement of tissue chromophore concentrations using photoacoustic spectroscopy: application to the measurement of blood oxygenation and haemoglobin concentration," *Phys. Med. Biol.* **52**(1), 141–168 (2007).
11. H. F. Zhang, K. Maslov, M. Sivaramakrishnan, G. Stoica, and L. V. Wang, "Imaging of hemoglobin oxygen saturation variations in single vessels in vivo using photoacoustic microscopy," *Appl. Phys. Lett.* **90**(5), 053901 (2007).
12. S. Sethuraman, J. H. Amirian, S. H. Litovsky, R. W. Smalling, and S. Y. Emelianov, "Spectroscopic intravascular photoacoustic imaging to differentiate atherosclerotic plaques," *Opt. Express* **16**(5), 3362–3367 (2008).

13. M. L. Li, J. T. Oh, X. Xie, G. Ku, W. Wang, C. Li, G. Lungu, G. Stoica, and L. V. Wang, "Simultaneous molecular and hypoxia imaging of brain tumors in vivo using spectroscopic photoacoustic tomography," *Proc. IEEE* **96**(3), 481–489 (2008).
14. D. Razansky, C. Vinegoni, and V. Ntziachristos, "Multispectral photoacoustic imaging of fluorochromes in small animals," *Opt. Lett.* **32**(19), 2891–2893 (2007).
15. D. Razansky, M. Distel, C. Vinegoni, R. Ma, N. Perrimon, R. W. Köster, and V. Ntziachristos, "Multispectral opto-acoustic tomography of deep-seated fluorescent proteins in vivo," *Nat. Photonics* **3**(7), 412–417 (2009).
16. A. De La Zerda, C. Zavaleta, S. Keren, S. Vaithilingam, S. Bodapati, Z. Liu, J. Levi, B. R. Smith, T. J. Ma, O. Oralkan, Z. Cheng, X. Chen, H. Dai, B. T. Khuri-Yakub, and S. S. Gambhir, "Carbon nanotubes as photoacoustic molecular imaging agents in living mice," *Nat. Nanotechnol.* **3**(9), 557–562 (2008).
17. M. Eghtedari, A. Oraevsky, J. A. Copland, N. A. Kotov, A. Conjusteau, and M. Motamedi, "High sensitivity of in vivo detection of gold nanorods using a laser optoacoustic imaging system," *Nano Lett.* **7**(7), 1914–1918 (2007).
18. P. C. Li, C. R. C. Wang, D. B. Shieh, C. W. Wei, C. K. Liao, C. Poe, S. Jhan, A. A. Ding, and Y. N. Wu, "In vivo photoacoustic molecular imaging with simultaneous multiple selective targeting using antibody-conjugated gold nanorods," *Opt. Express* **16**(23), 18605–18615 (2008).
19. V. Ntziachristos, and D. Razansky, "Molecular imaging by means of multispectral optoacoustic tomography (MSOT)," *Chem. Rev.* **110**(5), 2783–2794 (2010).
20. H. P. Brecht, R. Su, M. Fronheiser, S. A. Ermilov, A. Conjusteau, and A. A. Oraevsky, "Whole-body three-dimensional optoacoustic tomography system for small animals," *J. Biomed. Opt.* **14**(6), 064007 (2009).
21. R. Ma, A. Taruttis, V. Ntziachristos, and D. Razansky, "Multispectral optoacoustic tomography (MSOT) scanner for whole-body small animal imaging," *Opt. Express* **17**(24), 21414–21426 (2009).
22. J. Gamelin, A. Maurudis, A. Aguirre, F. Huang, P. Guo, L. V. Wang, and Q. Zhu, "A real-time photoacoustic tomography system for small animals," *Opt. Express* **17**(13), 10489–10498 (2009).
23. K. H. Song, and L. V. Wang, "Noninvasive photoacoustic imaging of the thoracic cavity and the kidney in small and large animals," *Med. Phys.* **35**(10), 4524–4529 (2008).
24. A. Buehler, E. Herzog, D. Razansky, and V. Ntziachristos, "Video rate optoacoustic tomography of mouse kidney perfusion," *Opt. Lett.* **35**(14), 2475–2477 (2010).
25. Laser Institute of America, "American National Standard for Safe use of Lasers ANSI Z136. 1-2000," *American National Standard Institute* (2000).
26. D. Razansky, J. Baeten, and V. Ntziachristos, "Sensitivity of molecular target detection by multispectral optoacoustic tomography (MSOT)," *Med. Phys.* **36**(3), 939–945 (2009).
27. A. Rosenthal, D. Razansky, and V. Ntziachristos, "Fast semi-analytical model-based acoustic inversion for quantitative optoacoustic tomography," *IEEE Trans. Med. Imaging* **29**(6), 1275–1285 (2010).
28. R. A. Kruger, D. R. Reinecke, and G. A. Kruger, "Thermoacoustic computed tomography--technical considerations," *Med. Phys.* **26**(9), 1832–1837 (1999).
29. C. K. Zarins, D. P. Giddens, B. K. Bharadvaj, V. S. Sottiurai, R. F. Mabon, and S. Glagov, "Carotid bifurcation atherosclerosis. Quantitative correlation of plaque localization with flow velocity profiles and wall shear stress," *Circ. Res.* **53**(4), 502–514 (1983).
30. K. H. Song, C. Kim, K. Maslov, and L. V. Wang, "Noninvasive in vivo spectroscopic nanorod-contrast photoacoustic mapping of sentinel lymph nodes," *Eur. J. Radiol.* **70**(2), 227–231 (2009).
31. A. Agarwal, S. W. Huang, M. O'Donnell, K. C. Day, M. Day, N. Kotov, and S. Ashkenazi, "Targeted gold nanorod contrast agent for prostate cancer detection by photoacoustic imaging," *J. Appl. Phys.* **102**(6), 064701 (2007).
32. S. S. Chang, C. W. Shih, C. D. Chen, W. C. Lai, and C. R. C. Wang, "The shape transition of gold nanorods," *Langmuir* **15**(3), 701–709 (1999).
33. C. L. Didychuk, P. Ephrat, A. Chamson-Reig, S. L. Jacques, and J. J. L. Carson, "Depth of photothermal conversion of gold nanorods embedded in a tissue-like phantom," *Nanotechnology* **20**(19), 195102 (2009).
34. F. A. Jaffer, P. Libby, and R. Weissleder, "Molecular imaging of cardiovascular disease," *Circulation* **116**(9), 1052–1061 (2007).

1. Introduction

Optoacoustic imaging is emerging as a powerful technique for resolving tissue chromophores at the high spatial resolution provided by ultrasound detection [1,2]. The method is based on the detection of ultrasonic waves generated by thermoelastic expansion of tissues arising from transient temperature increases due to the absorption of nanosecond light pulses. The amplitude of the generated ultrasound waves depends on the local light fluence and optical absorption properties of the tissue. Since scattering of ultrasonic waves in tissue is weak compared to scattering of light, optoacoustic imaging is able to combine the high contrast obtained from optical absorption with the high resolution of ultrasonic detection.

Optoacoustic imaging has a natural sensitivity to hemoglobin, the latter being the major absorber of light in tissues. In consequence, optoacoustic imaging has been employed to visualize vascularization, which is relevant to the understanding of tissue physiology or angiogenesis responses [1,3–7]. While intravital optical microscopy can typically visualize

vascularization with superior resolution (1–10 μm , depending on the technique) to optoacoustics (15 μm with optical resolution photacoustic microscopy [8]), the definitive advantage of optoacoustic imaging is its ability to visualize much deeper in tissues (> 1 cm) compared to the penetration limits of, for example, multi-photon microscopy (0.4–1 mm) or optical coherence tomography (< 2 mm) [9]. While the resolution attainable with optoacoustic imaging degrades with penetration depth because of increasing ultrasound attenuation with frequency in tissue, the strong scattering of light in tissue means that the resolution of pure optical techniques degrades far faster with depth [2].

Using the spectral differentiation capabilities of multispectral optoacoustic tomography (MSOT), the determination of oxygenation states of hemoglobin has been shown possible [10,11]. Detection of atherosclerotic plaque composition based on intrinsic tissue composition has additionally been suggested using an intravascular optoacoustic catheter system [12]. Crucially, MSOT has shown the ability to resolve molecular agents, such as fluorochromes [13,14] and fluorescent proteins [15], and other chromophoric agents [16–19] in tissues.

Macroscopic optoacoustic tomography requires implementations that volumetrically illuminate tissues and utilize detectors sensitive to lower frequency ranges, which are attenuated less in tissues, to detect signals from deep below the skin surface. Using mechanical scanning of either animal or transducer, such approaches have shown visualization of absorbing tissue structures [1,20–22]. In this work we investigated the ability of optoacoustic imaging to resolve structures in mice that are commonly involved with cardiovascular disease (CVD), namely the carotid arteries, the aorta and the cardiac wall. Comparable approaches in small animal optoacoustic imaging have, for example, shown unidentified structures in a microscopic field of view in the heart region [4], macroscopic imaging of the rat thorax (post mortem) with an acquisition time of over 10 minutes [23], 3D imaging of the abdominal aorta in mice with an acquisition time of several minutes [20], or real-time imaging limited by geometry to visualizing the top of the brain [22]. We utilized a novel MSOT system that was designed for functional and molecular studies of tissue. The scanner is ideally suited for studying CVD features in mouse models as it attains real-time imaging features appropriate for imaging physiological responses while its multispectral capability enables imaging of various exogenous chromophoric agents with distinct spectral features. To gain insights on possible imaging challenges we characterized the ultrasound attenuation through murine rib cages in order to elucidate potential sources of signal degradation. Correspondingly we demonstrate herein previously undocumented imaging capabilities yielding high resolution transverse slices with identifiable CVD related structures and real-time visualization of gold nanorod circulation in blood vessels of the neck. In the following we describe the methods utilized, showcase the most pertinent results of the study and discuss limitations and the outlook of the technology in CVD research and clinical translation.

2. Materials and methods

2.1 Real-time MSOT experimental setup for in-vivo imaging

Figure 1 illustrates the experimental setup used in this paper, which is also described in Ref [24]. It consists of a tunable optical parametric oscillator (OPO) pumped by an Nd:YAG laser (Opotek Inc., Carlsbad, CA) with a near-infrared (700–900nm) tuning range. The laser pulse duration is below 10 ns and the pulse repetition frequency is 10 Hz, defining the maximum possible frame-rate. The beam is coupled into a fiber bundle that is divided into 10 arms on the output side which illuminate the animal from multiple angles on the imaging plane. The custom fiber bundle assembly (CeramOptic Industries, Inc., East Longmeadow, MA) consists of approximately 630 fibers, each with a fused silica core of 179 μm diameter and a numerical aperture of 0.37. The input end of the fiber bundle is fused in silica and has an active diameter of 5 mm. The fibers are then divided into 10 identical arms, each having an active diameter of 1.74 mm at the output. The assembly has a total length of approximately 2 m and has been measured to have an overall efficiency of approximately 80% in the wavelength range from

700 to 850 nm. The pulse energy at the OPO output (before the fiber bundle) in the experiments we performed was below 85 mJ at 740 nm, the peak of the OPO tuning curve. The laser spot size from each fiber bundle output on the animal skin surface was estimated using burn paper to have an area of approximately 0.36 cm^2 , resulting in an estimate of the fluence on skin of 19 mJ/cm^2 at 740 nm, assuming an 80% fiber bundle efficiency and a pulse energy at the OPO output of 85 mJ. This value is below the maximum permissible exposure (MPE) of 24 mJ/cm^2 at 740 nm [25] as well as the 22.4 mJ/cm^2 MPE at 725 nm. These are the limiting cases since the other (longer) wavelengths used here correspond to lower pulse energies from the OPO as well as higher MPE values. A custom-made piezocomposite ultrasonic transducer array (Imasonic SAS, Voray, France) with 64 elements having a central frequency of 5 MHz and a bandwidth (-6 dB) of 57% is used for detection. The elements are arranged in one row forming a spherical concave array covering 172° with a mechanical focal distance of 4 cm. Each element has dimensions of 1.88 mm by 15 mm with an inter-element spacing of 0.1 mm. As a whole, these dimensions allow the transducer array to be considered as being cylindrically focused on the imaged plane. The time-resolved signals are digitized by an acquisition system consisting of an 18 slot PXI chassis (NI PXI-1045, National Instruments Corp., Austin, TX) containing 8 digitizer boards (NI PXI-5105, National Instruments Corp.) with 8 channels each, giving a total of 64 channels. The signals are acquired at 60 MSps and 12 bit digital resolution. An embedded controller (NI PXI-8106, National Instruments Corp.) in the same chassis is used for coordinating the instrumentation via a LabVIEW (National Instruments Corp.) interface. As a whole, the acquisition system is capable of acquiring data at the 10 frames-per-second limit imposed by the laser repetition rate. The transducer array and fiber bundle outputs are submerged in a water bath. Mice are placed in a prone position in a holder with a thin polyethylene membrane so that there is no direct contact between water and the mouse. This holder is positioned in the water bath so that the mouse is centered around the focal point of the transducer array. The laser beams and ultrasonic transducer array are in fixed position for all data acquisitions, whereas the animal being imaged can be translated through the imaging plane using a linear stage (NRT 150/M, Thorlabs GmbH, Dachau, Germany) to enable imaging of multiple transverse slices.

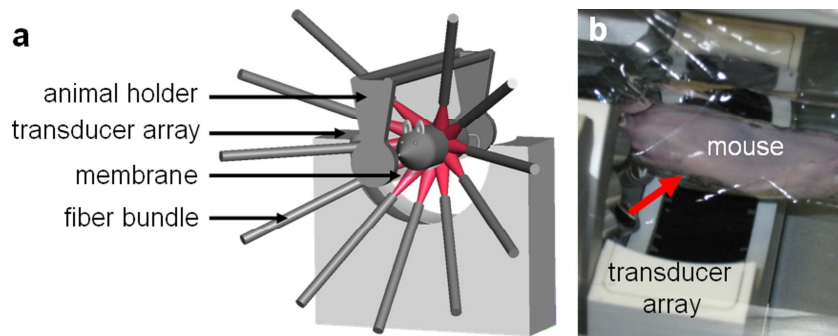


Fig. 1. a: Schematic of the experimental setup. b: The setup during measurement of a mouse, where the red arrow indicates the illumination path from a fiber bundle output to the mouse.

2.2 Gold nanorods

Commercially available gold nanorods (AuNR) with an absorption peak in the near-infrared (Ntracker 30-PM-780, Nanopartz Inc., Loveland, CO) were used to demonstrate our ability to detect exogenous contrast agents. The AuNR have, according to the manufacturer, an absorption peak around 780 nm, and a per particle width of 10 nm and length of 38 nm. A proprietary polymer coating gives the nanorods lengthened circulation times. The absorption spectrum of the AuNR is shown in Fig. 2.

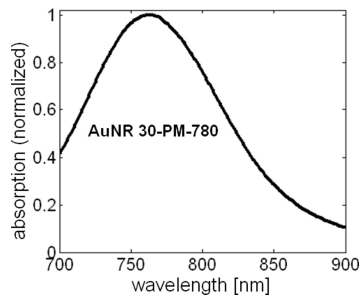


Fig. 2. The normalized absorption spectrum of the AuNR.

2.3 Animal handling and imaging

Procedures involving animals and their care were conducted in conformity with the authors' institutional guidelines complying with national and international laws and regulations. Experimental protocols were reviewed and approved by the Bavarian Animal Research Authority. Adult mice (CD-1[®] and CD-1[®] Nude, Charles River Laboratories, Sulzfeld, Germany) imaged *in vivo* were anesthetized using ketamine/xylazine and shaved (if necessary) prior to imaging in the experimental MSOT setup and placed on the polyethylene membrane in the system in a prone position such that the transducer array faced the ventral side of the animals. For real-time operation, each two-dimensional optoacoustic image obtained utilized raw data corresponding to a single laser pulse. Mice were linearly translated in front of the detector in order to image different positions at the neck and thorax. For gold nanorod measurements, mice were scanned at 5 excitation wavelengths (725 nm, 750 nm, 775 nm, 800 nm, 825 nm) using 10 signal averages per slice to serve as a control prior to agent injection. Following these reference measurements, 200 μ l of AuNR at a concentration of 13 nM (of the nanorods themselves, corresponds to a number density of 7.8 fl^{-1}) were intravenously injected via the tail vein, in order to evaluate the possibility of real-time dynamic imaging of an exogenous agent. During agent injection, data from a slice through the neck were continuously acquired over 110 s at 780 nm. Following the dynamic measurement, the same slice was again scanned at 5 excitation wavelengths (725 nm, 750 nm, 775 nm, 800 nm, 825 nm) using 10 signal averages in order to investigate the ability to spectrally differentiate the particles from background signals.

Directly after imaging the mice were euthanized and frozen. For anatomical validation of the optoacoustic images, color photographs were taken during sectioning in a cryostat (CM 1950, Leica Microsystems, Wetzlar, Germany).

2.4 Murine rib cage ultrasound measurements

Ex vivo measurements were independently performed in an optoacoustic testbed, illustrated in Fig. 3a, to characterize the ultrasound attenuation characteristics of the murine rib cage. While the MSOT imaging performance of blood vessels in the neck, for example the carotid arteries imaged in this paper, depends primarily on target size and depth [26], rib cage attenuation may affect cardiac imaging and was therefore characterized herein in conditions similar to those in optoacoustic experiments. Intact rib cages, pictured in Fig. 3b, were excised from two freshly sacrificed adult CD-1 mice and placed in the testbed. A broadband ultrasound signal was generated by illuminating a carbon rod of approximately 0.5 mm diameter with a nanosecond laser pulse. The signals were measured using a piezoelectric ultrasound transducer (Model V382, Panametrics NDT, Waltam, MA) with a central frequency of 3.5 MHz, a bandwidth of 76%, cylindrical focus (focal length 3.8 cm) and an element diameter of 13 mm. This wide diameter allowed for the signal to be measured simultaneously through a range of different regions in the rib cage similar to the conditions in animal experiments. The time-resolved signals detected by the transducer were digitized and averaged (2000 times) by an embedded oscilloscope card (NI PCI-5122, National Instruments Corp., Austin, TX) at 100

Msp and 14 bit digital resolution. The rib cages were translated manually in the height direction to take 4 optoacoustic measurements for each of the 2 rib cages. Baseline measurements were taken with the rib cages removed. The average of the power spectrum of each of the signals through the rib cages was compared to the baseline power spectrum to calculate the rib cage insertion loss.

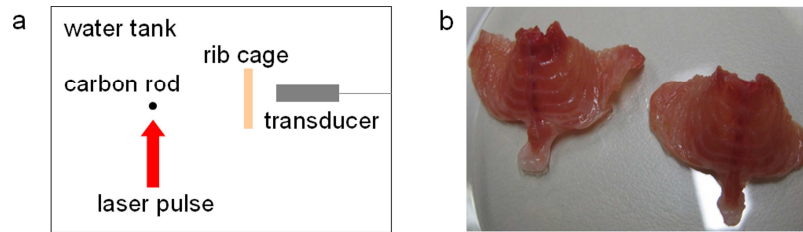


Fig. 3. a: Schematic of testbed used for rib cage ultrasound measurements. b: Rib cages excised from mice.

2.5 Image reconstruction

The images shown in this paper were reconstructed using a linear model-based inversion [27], or using a filtered backprojection algorithm [28]. In the case of the model-based inversion, once the model matrix corresponding to the fixed measurement geometry had been generated, it took approximately 14 seconds to produce a 240x240 pixel image on a PC (Intel 3 GHz Core 2 Duo with 6 GB of RAM) using Matlab software (The Mathworks Inc, Natick, MA). Images displayed in real-time on the measurement system were reconstructed using the backprojection algorithm, which took under 100 ms to produce a lower resolution image.

In addition, linear spectral unmixing was applied for multispectral detection of AuNR [15]. For each pixel in the image, the method fits the measured optoacoustic spectrum, normalized for variations in laser energy per wavelength, to the known absorption spectra of oxy and deoxy-hemoglobin and that of the AuNR. The fitting is performed by least-squares on the set of 5 linear equations, corresponding to the 5 measured wavelengths, generated for the 4 fitted spectra (3 known chromophore spectra and 1 constant spectrum). Even without correction for fluence variations inside the tissue, the image consisting of fitted AuNR spectral contributions yields a spatial map of the detected signal attributable to the agent.

3. Results

3.1 Imaging the aorta and carotids

Figure 4 shows optoacoustic images of the upper thorax and neck (750 nm excitation). The images reveal clear signals from the aortic arch and the carotid arteries captured in transverse (axial) slices. In particular, Fig. 4a shows a slice through the top part of the aortic arch and Fig. 4b shows a slice approximately 2 mm above the aortic arch, revealing the innominate artery and the left common carotid artery. Figure 4c shows the carotid arteries near the point of bifurcation, a frequent location for atherosclerotic plaque formation [29], approximately 10 mm in the cranial direction from the aortic arch. Here the carotid arteries are at a depth of approximately 5 mm from the ventral skin surface. Figures 4d-f show color photographs of cryosections at corresponding slices confirming the anatomical structures seen in the optoacoustic images. The images also show strong contrast from blood vessels apart from the arteries mentioned, for example the superior vena cava.

The carotid arteries in mice have a small diameter on the order of hundreds of micrometers and are shielded by absorbing structures, such as the large veins of the neck, thus presenting a challenging imaging target. Nevertheless, as evident in the images, the real-time optoacoustic scanner described herein, equipped with multi-angle illumination and detection, resolves these structures with sufficient contrast.

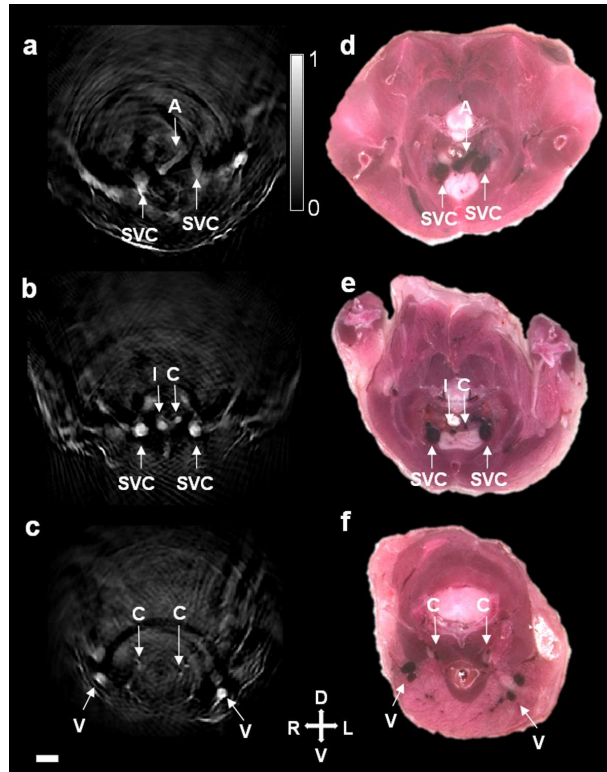


Fig. 4. Transverse optoacoustic slices of arteries in the upper thorax and neck (750 nm excitation). a: Slice through top of aortic arch. Aortic arch labeled 'A'. Left and right superior vena cava labeled 'SVC'. b: Slice showing arteries just above aortic arch. Innominate artery labeled 'I', left common carotid artery labeled 'C', left and right superior vena cava labeled 'SVC'. c: Slice approximately 10 mm cranially from aortic arch showing carotid arteries near bifurcation. Carotid arteries labeled 'C', veins branching from external jugular vein 'V'. Scale bar: 2 mm. d-f: Photographs of cryosections showing corresponding anatomical structures to the images in a-c respectively.

3.2 Real-time imaging of circulating gold nanorods

Figure 5 summarizes results from imaging AuNR, which examine the ability of the system to perform dynamic imaging. Figure 5a-c show single-pulse images (no signal averaging) from a series of acquisitions at the nominal peak absorption wavelength of the AuNR, 780 nm, made before (Fig. 5a), during (Fig. 5b), and after (Fig. 5c) the intravenous administration of the agent. As observed in the images, the amplitude of the signal collected from the blood vessels imaged, in particular the external jugular veins at the front of the neck, increases after AuNR injection. Because of the high absorption of light in these large blood vessels, the signal from the front of the vessels, where the excitation light is not yet attenuated, dominates the images.

[Media 1](#) shows an animation consisting of individual images acquired during agent administration, demonstrating the attained contrast increase dynamically. As observed, gold nanorods are detectable while circulating in the blood vessels. An estimation of the average AuNR concentration in the bloodstream can be calculated by multiplying the initial concentration injected by the injected volume and dividing by a typical value for the volume of blood in a mouse: $C = \frac{3 \text{ nM} \times 200 \mu\text{l}}{2 \text{ ml}} = 1.3 \text{ nM}$ (number density 0.78 fl^{-1}).

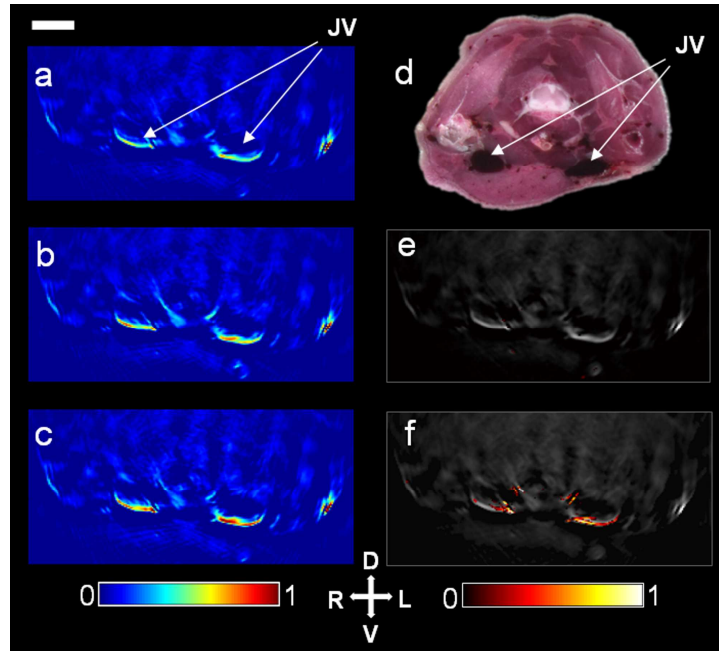


Fig. 5. Optoacoustic detection of AuNR. Jugular veins labeled 'JV'. a: Single-pulse transverse slice through neck prior to injection. b: The same slice during injection of AuNR. c: And 10 s after finishing the injection of AuNR. (Media 1) shows the captured frames in animation, frame spacing approximately 1s. d: Photograph of cryosection showing anatomical correspondences. e: MSOT image before injection. f: MSOT image post injection showing multispectrally resolved distribution of AuNR overlaid on a single wavelength image. Scale bar 3 mm.

3.3 Multispectral imaging of circulating gold nanorods

Figure 5e and 5f summarize results from MSOT imaging of AuNR aiming at investigating whether detection is possible based on its spectral profile. This is in contrast to the detection of AuNR based on signal differences it imparts on background measurements after its administration in a time-wise fashion as described in the previous section. Figure 5e and 5f show MSOT images of the mouse neck before and after injection respectively. Here, the multispectrally resolved signals from AuNR are overlaid on single wavelength images (775 nm) showing the relevant anatomical features. As can be clearly seen from the images, MSOT resolves the circulating nanorods in the blood vessels with high contrast as opposed to the control image from before injection. The spatial location of the resolved AuNR signal corresponds well to the regions of increased contrast in the real-time imaging during injection. This result highlights the ability of MSOT to resolve exogenous agents *in vivo* at high resolution without need for a baseline measurement, based on their distinct spectral profile over the background tissue absorption spectrum.

3.4 Heart imaging

To examine whether cardiac tissues are also visible in a noninvasive manner by optoacoustics, we performed imaging at the heart level. Figure 6a and 6b show *in vivo* images of the anterior heart wall generated from single laser pulses (740 nm) at different points in the cardiac cycle. The images also demonstrate other structures, for example the sternum, small blood vessels behind the ribs, and part of the blood pools inside the left and right ventricles. The depth of the heart (approximately 2 mm) and thickness of the heart wall (approximately 0.8 mm) agree with expected values in our experience of mouse anatomy. Internal structures of the ventricles or the posterior heart wall are not clearly visible at present. This is likely due to the angled illumination utilized in this approach that is not optimal for imaging at the heart level, where

the noncylindrical shape of the mouse means that the laser beams do not all illuminate the skin surface in the imaged plane. The high attenuation of light in the blood-filled ventricles may also be a limiting factor, although typically the ventricles empty of blood in every systole, therefore it would be in principle possible to trigger the method appropriately to reduce these effects. Another limiting factor is the current inability of the inversion models used to account for acoustic reflections in the heart-lung interfaces and other tomographic artifacts produced by the lungs.

The information shown in the optoacoustic images in Fig. 6a and 6b is acquired within the time that it takes for the optoacoustically-generated signals to propagate from the animal toward the detectors, i.e. on the order of 50 μ s. This results in images free of motion artifacts and the possibility of resolving the motion of the heart itself. Since the repetition frequency of the measurement setup is not equal to that of the heartbeat, the images captured show the heart in various stages of the cardiac cycle, such that subsequent images can be grouped together into an animation, as shown in Media 2. In cases where a multispectral approach is used, for example to resolve exogenous contrast agents, signals from multiple pulses must be used to average out the motion per wavelength (in the absence of a relevant heartbeat triggering method). In this case, there is some motion-blur in the image from the heartbeat and breathing, but as shown in Fig. 6c, where images from 41 single-pulse frames are averaged, the image quality, despite obvious motion artifacts, is still good enough for the heart wall to be distinguished to some extent from surrounding tissue. In Fig. 6d, the image has been averaged from 22 manually selected frames, discarding those showing ventricular systole. This selection further improves image quality by reducing motion artifacts, and can conceivably be automated in the future using standard image processing techniques.

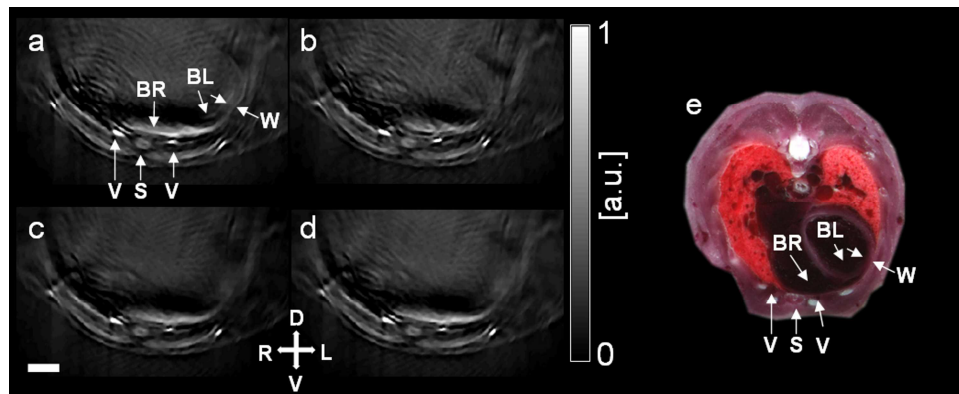


Fig. 6. Optoacoustic heart imaging (740 nm excitation). a: Single-pulse image showing heart wall ('W'). Also visible are signals from blood inside the left and right ventricles ('BL' and 'BR') and the sternum ('S') and veins ('V'). (Media 2) shows animation of further frames of the heart in motion. b: Single-pulse image taken during ventricular systole. c: Average image over 41 pulses showing motion-blur. d: Average image over 22 selected frames showing reduced motion-blur. Scale bar 2 mm (applies to optoacoustic images). e: Photograph of cryosection through the heart of a mouse showing features corresponding to optoacoustic images.

Finally, Fig. 7 corroborates the imaging findings by summarizing results from the attenuation measurements of two murine rib cages. Figure 7a shows optoacoustic signals in the presence and the absence of a murine rib cage. The signal acquired through the rib cage demonstrates slight attenuation compared to the baseline (water) measurement, but is otherwise very similar in amplitude and shape. Figure 7b shows the insertion loss of the rib cages calculated from the measurement data. Even at a frequency of 3.5 MHz, corresponding to a spatial resolution of 215 μ m, there is only an attenuation of approximately 3 dB. This shows that only moderate attenuation is expected from the rib cage, leading to the conclusion that cardiac optoacoustic measurements of mice are not expected to suffer from insufficient

signal-to-noise ratio as long as signals from the heart are acquired on the ventral side, i.e. not through the lungs.

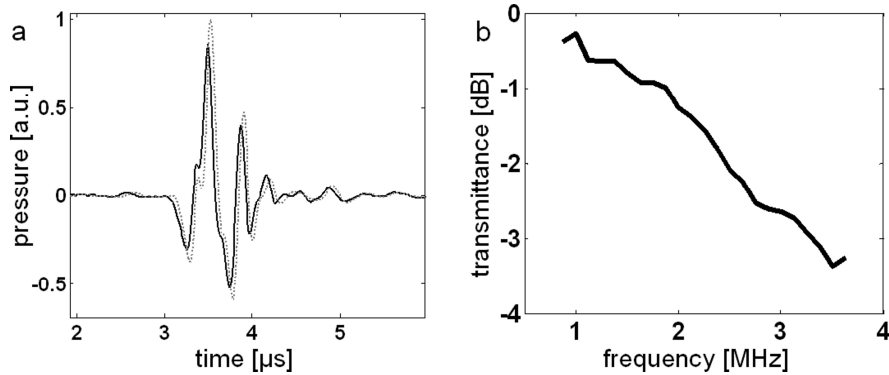


Fig. 7. a: Measured ultrasound signals. Dotted: baseline, solid: through rib cage. b: Experimental ultrasound transmission through the murine rib cage plotted against frequency.

4. Discussion and conclusions

We have demonstrated in this paper a platform to image several important aspects of the cardiovascular system macroscopically and noninvasively in mice, including the heart, the aorta and the carotid arteries, *in vivo* and in real-time. The ability of optoacoustic imaging to resolve these anatomical structures, which play a major role in the research and diagnosis of cardiovascular disease, enables promising applications of the technique in this field. In connection to this we have shown contrast enhancement using gold nanorods as an exogenous agent with a view to combining, in the future, the multispectral visualization of exogenously administered agents with the intrinsic anatomical imaging capabilities of optoacoustics to provide powerful molecular cardiovascular imaging. The problem of high ultrasound attenuation posed by the lungs is overcome by acquiring the ultrasound signals through the front of the chest where the rib cage has been experimentally shown to pose no great obstacle to ultrasound. Real-time optoacoustic monitoring of cardiovascular dynamics in the microscopic domain has been reported on mice showing absorbers at a high frame rate [4]. However, to our knowledge, there is no optoacoustic system up till now reported capable of noninvasive macroscopic imaging of the small animal cardiovascular system in real-time. Our results show the heart in detail, able to clearly distinguish the anterior heart wall from blood inside the heart chambers. We have demonstrated dynamic imaging, free of motion artifacts from the heartbeat or breathing, which can be applied for assessing cardiac function. For multispectral imaging of the heart, where motion (due to respiration or heartbeat) between different wavelengths requires, in the absence of cardiac or respiratory synchronization or triggering methods, averaging of multiple signals, we have shown that anatomical structures can still be recognized. Manual selection of images at similar points in the cardiac cycle improves averaged image quality.

In addition to the possibility to extract morphological information from the images, exogenous contrast agents highlighting biological targets in the myocardium would provide a method for molecular imaging of the heart. Here, we have been able to detect gold nanorods circulating in the bloodstream, both by dynamic imaging of the resulting contrast enhancement at a single wavelength corresponding to the peak absorption of the agent, and by use of the MSOT technique to resolve the unique spectral signature of the agent *in vivo*. Gold nanorods show high absorption (molar extinction coefficient on the order of $10^8 \text{ M}^{-1}\text{cm}^{-1}$) with absorption peaks tunable by adjusting their aspect ratios, making them especially suitable for use in optoacoustic imaging and MSOT in particular. They have been used purely as an optoacoustic contrast enhancing agent [17,30] and have been conjugated to targeting ligands for molecular imaging [31], with the additional possibility of visualization of multiple

biological targets with gold nanorods of different aspect ratios and thus distinguishable absorption peaks [18]. Gold nanorods are known to change shape (and therefore absorption properties) due to melting from the heating energy of pulsed laser [32,33], possibly limiting the fluence and number of pulses used for quantitative optoacoustic imaging; this limitation requires further investigation for specific nanorod dimensions and imaging scenarios. Nevertheless, the resolving power of MSOT combined with gold nanorods demonstrated in our imaging platform indicates the feasibility of cardiovascular molecular imaging using gold nanorods conjugated to targeting ligands, promising such applications as visualization of infarct healing, inflammation in atherosclerotic plaques, tracking of stem cell therapy and many others [34]. Furthermore, the macroscopic imaging demonstrated here on mice indicates that it may be possible to apply these methods to clinical diagnosis of CVD, for example on such targets as the carotid arteries in the human neck.

Acknowledgements

V. N. acknowledges support from the European Research Council through an Advanced Investigator Award. D. R. acknowledges support from the German Research Foundation (DFG) Research Grant (RA 1848/1).